Analytical model for the source resistance in advanced $In_xGa_{1-x}As/In_{0.52}Al_{0.48}As$ quantum-well high-electron-mobility transistors

Ji-Hoon Yoo[1], Jae-Hak Lee[1], Yong-Hyun Kim[2], Sang-Kuk Kim[2], Jacob Yun[2], Ted Kim[2], In-Geun Lee[1] and *Dae-Hyun Kim[1]

[1]*School of Electronic and Electrical Engineering, Kyungpook National University, Daegu, Korea* and [2]*QSI, Cheon-An, South Korea.*

Keywords: $In_xGa_{1-x}As$, Source resistance, TLM, HEMT

Abstract (Times New Roman Font, Bold, Size 10)

We present a fully analytical model for the source resistance (R_S) in $In_xGa_{1-x}As$ quantum-well high-electron mobility transistors based on a three-layer TLM system. The proposed R_S model in this work was derived by solving the coupled 2nd order differential equations for each current component in a non-alloyed source drain ohmic structure with appropriate boundary conditions, requiring only six physical and geometrical parameters, such as ohmic contact resistivity (ρ_c), barrier tunneling resistivity ($\rho_{barrier}$), sheet resistances of the cap and channel regions (R_{sh_cap} and R_{sh_ch}), side-recessed length (L_{side}) and gate-to-source length (L_{gs}). We fabricated two different TLM structures to extract each model parameter, such as *cap-TLM* and *recessed-TLM* patterns. The developed R_S model in this work was in excellent agreement with the R_S values measured from the two TLM devices and previously reported short-L_g HEMT devices. The model revealed that the barrier tunneling resistivity already played a critical role in reducing the value of R_S in state-of-the-art HEMTs. Unless the barrier tunneling resistivity is reduced considerably, innovative engineering on the ohmic contact characteristics and the reduction on gate-to-source spacing (L_{gs}) would only marginally improve the device performance.

INTRODUCTION

The evolving sixth-generation (6G) wireless communication technologies demand higher operating frequencies of approximately 300 GHz with data rates approaching 0.1 Tbps [1,2]. To meet this urgent requirement, transistor technologies must be engineered to sustain the evolution of digital communication systems, guided by Edholm's law [3]. Among various transistor technologies, indium-rich $In_xGa_{1-x}As$ quantum-well (QW) high-electron-mobility transistors (HEMTs) on InP substrates provide the best balance of current-gain cutoff frequency (f_T) and maximum oscillation frequency (f_{max}), and the lowest noise figure characteristics from the microwave to sub-millimeter-wave regions [4–8]. These transistors adopt a combination of L_g scaling down to sub-30 nm, enhancement of the channel carrier transport by incorporating the indium-rich channel design, and reduction of all parasitic components.

Among various parasitic components, it is imperative to minimize the source resistance (R_S) to bring up the superior intrinsic performance of the $In_xGa_{1-x}As$ QW channel [9,10], demanding an analytical and physical model for the source resistance. Considering state-of-the-art $In_xGa_{1-x}As$ HEMT technologies [11–14], source and drain contacts have been created with a non-alloyed metal stack of Ti/Pt/Au with a source-to-drain spacing (L_{ds}) between 1 µm and 0.5 µm. Historically, R_S has been minimized by improving ohmic contact characteristics to reduce the ohmic contact resistivity (ρ_c) [15] and shrinking the gate-to-source spacing (L_{gs}) using a self-aligned gate architecture [16,17]. However, it is very challenging to reduce R_S to below 100 Ω·µm, because of the tunneling resistance component between the heavily doped $In_{0.53}Ga_{0.47}As$ capping layer and the $In_xGa_{1-x}As$ QW channel layer through the $In_{0.52}Al_{0.48}As$ barrier layer. To understand the limit of R_S in HEMTs in an effort to reduce R_S, a sophisticated and comprehensive model must be developed for R_S in state-of-the art HEMTs, rather than the simple lumped-elements-based one-layer model [18,19].

Previously, two-layer system-based R_S model was developed by Feuer [20], which can explain the alloyed ohmic contact structures with two different contact resistances: one was associated with a heavily doped GaAs capping layer and the other with an undoped GaAs QW channel layer. However, the two-layer system-based model could not fully explain R_S with non-alloyed ohmic structure. Herein, we present a fully analytical and physical model for R_S in advanced HEMTs, demanding only six physical and geometrical parameters. The model consists of three different regions: (i) an analytical three-layer TLM for the source electrode region, (ii) an analytical TLM for the access region and (iii), a one-layer transmission-line model (TLM) for the side-recess region, to accurately predict a value of R_S in a given HEMT structure and identify dominant components to further minimize R_S. To do so, we proposed and fabricated two different types of TLM structures to experimentally extract each model parameter of R_S. The proposed model in this work is in excellent agreement with the measured values of R_S from the fabricated recessed TLM test structures, as well as recently reported advanced HEMTs. Most importantly the findings in this work reveal that the barrier tunneling resistivity is a bottleneck for further reductions of R_S in advanced HEMTs.

ANALYTICAL MODEL FOR THE SOURCE RESISTANCE

Figure 1 (a) and **(b)** show the cross-sectional schematic and TEM images of advanced $In_xGa_{1-x}As$ QW HEMTs on an InP substrate [4]. They adopt non-alloyed S/D ohmic contacts such as a metal stack of Ti/Pt/Au with contact resistance (R_C) values between 10 Ω·μm and 20 Ω·μm. Carrier transfer from the cap to channel by a tunneling mechanism through an $In_{0.52}Al_{0.48}As$ barrier layer. To model R_S, a comprehensive transport mechanism from the source ohmic electrode to the $In_xGa_{1-x}As$ QW channel via the $In_{0.53}Ga_{0.47}As$ cap and $In_{0.52}Al_{0.48}As$ barrier layers must be considered in a distributed manner, when will be discussed next.

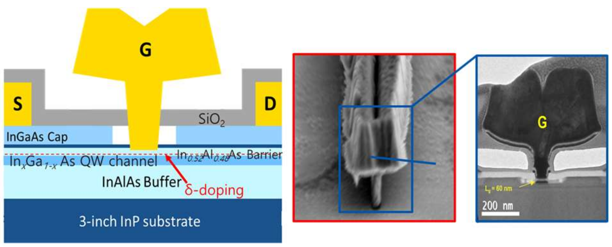

(a) (b)

Figure 1 (a) Cross-sectional schematic, and **(b)** TEM images of advanced $In_xGa_{1-x}As$ QW HEMTs [4].

Figure 2 (a) illustrates a complete distributed equivalent circuit model for R_S, comprising three regions. One is the source ohmic electrode region (Region-I), where the electrons are injected from the ohmic metal to the $In_{0.53}Ga_{0.47}As$ cap and then to the $In_xGa_{1-x}As$ QW channel through the $In_{0.52}Al_{0.48}As$ barrier, which is governed by a three-layer TLM system. Another is the source access region (Region-II), where the electron transfer mechanism is governed by a cap-to-channel two-layer TLM system with transfer length ($L_{T\_barrier}$) given by $\sqrt{\rho_{barrier}/(R_{sh\_ch}+R_{sh\_cap})}$. The other is the side-recessed region (Region-III), where a simple one-layer model works. **Figure 2 (b)** highlights a differential segment at a given location in source model from x to $x+dx$.

Next, let us derive a fully analytical and physical expression for R_S. Given the coordinate system in **Fig. 2 (a)**, R_S can be determined by $V_{ch}(x=-L_{gs})/I_O$ from Ohm's law, including that the problem is how to express each current

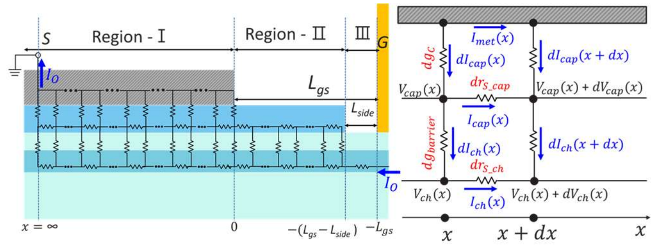

(a) (b)

Figure 2 (a) Equivalent circuit model of the source resistance in the advanced HEMTs and **(b)** differential segment from x to x +

component as a function of x such as $I_{ch}(x)$, $I_{cap}(x)$, and $I_{met}(x)$. In a given segment as highlighted in **Fig. 2 (b)**, we can define a differential contact conductance as $dg_c = (W_g/\rho_c) \times dx$, a differential barrier conductance as $dg_{barrier} = (W_g/\rho_{barrier}) \times dx$, a differential lateral cap resistance as $dr_{s\_cap} = (R_{sh\_cap}/W_g) \times dx$ and a differential lateral channel resistance as $dr_{s\_ch} = (R_{sh\_ch}/W_g) \times dx$. At location x, Kirchhoff's current and voltage laws yield, respectively

$$\frac{d^2 I_{met}(x)}{dx^2} = [R_{met}\cdot I_{met}(x) - R_{sh\_ch}\cdot I_{cap}(x)]\rho_c^{-1} \quad (1)$$

$$\frac{d^2 I_{ch}(x)}{dx^2} = [R_{sh\_ch}\cdot I_{ch}(x) - R_{sh\_cap}\cdot I_{cap}(x)]\rho_{barrier}^{-1} \quad (2)$$

$$I_{cap} = I_O - I_{met} - I_{ch} \quad (3)$$

These are coupled quadratic differential equations for three current components ($I_{ch}(x)$, $I_{cap}(x)$ and $I_{met}(x)$). From the general solution for these differential equations with existing six boundary conditions (listed in Table 1), we obtain an analytical expression for $I_{ch}(x)$, $I_{cap}(x)$, and $I_{met}(x)$ for both regions, as written in **Table 1.** The expression for $V_{ch}(x=-L_{gs})$ can then be derived. Although there exist several ways to express $V_{ch}(x=-L_{gs})$, it is useful to focus on the total voltage drop across the $In_xGa_{1-x}As$ QW channel from $x=-L_{gs}$ to $x=\infty$ in this work. From this,

$$V_{ch}(x=-L_{gs}) = \int I_{ch}(x)\cdot dr_{S\_ch}\; dx \quad (4)$$

The source resistance, defined as $V_{ch}(x=0)/I_O$, is

$$R_S = \frac{V_{ch}(x=-L_{gs})}{I_O} = \frac{W_g R_{sh\_ch}}{I_O}\int_{-L_{gs}}^{\infty} I_{ch}(x)\, dx \quad (5)$$

BCs	$I_{ch1}=I_O$ for $x=-L_{gs}$	$I_{met}=0$ for $-L_{gs}<x<0$	$I_{met}=I_O$ for $x=\infty$
	$I_{cap}(x=0^-)=I_{cap}(x=0^+)$	$I_{ch}(x=0^-)=I_{ch}(x=0^+)$	$\frac{dI_{ch}(x=0^-)}{dx} = -\frac{dI_{cap}(x=0^+)}{dx}$
Region-I	$\begin{bmatrix} I_{met} \\ I_{ch} \end{bmatrix} = \begin{bmatrix} v_{11} \\ v_{12} \end{bmatrix} C_1\,exp(-\sqrt{\lambda_1}x) + \begin{bmatrix} v_{21} \\ v_{22} \end{bmatrix} C_2\,exp(-\sqrt{\lambda_2}x) + \begin{bmatrix} I_O \\ 0 \end{bmatrix}$ $I_{cap} = I_O - I_{met} - I_{ch}$	Region-II	$I_{cap} = C_3\,exp\left(\frac{-x}{L_{T\_barrier}}\right) + C_4\,exp\left(\frac{x}{L_{T\_barrier}}\right) + \frac{R_{sh\_ch}}{R_{sh\_cap}+R_{sh\_ch}} I_O$ $I_{ch} = I_O - I_{cap}$
- λ_1 & λ_2 are eigenvalues of $A = \begin{bmatrix} \left(\frac{R_{sh\_cap}}{\rho_c}\right) & \left(\frac{R_{sh\_cap}}{\rho_c}\right) \\ \left(\frac{R_{sh\_cap}}{\rho_{barrier}}\right) & \left(\frac{R_{sh\_cap}+R_{sh\_cap}}{\rho_{barrier}}\right) \end{bmatrix}$ - $\begin{bmatrix} v_{11} \\ v_{12} \end{bmatrix}$ & $\begin{bmatrix} v_{21} \\ v_{22} \end{bmatrix}$ are their corresponding eigenvectors			$\begin{bmatrix} C_1 \\ C_2 \\ C_3 \\ C_4 \end{bmatrix} = \begin{bmatrix} 0 & 0 & exp\left(\frac{L_{gs}}{L_{T\_barrier}}\right) & exp\left(\frac{-L_{gs}}{L_{T\_barrier}}\right) \\ v_{12} & v_{22} & 1 & 1 \\ v_{11} & v_{21} & 0 & 0 \\ -\sqrt{\lambda_1}v_{12} & -\sqrt{\lambda_2}v_{22} & -\frac{1}{L_{T\_barrier}} & \frac{1}{L_{T\_barrier}} \end{bmatrix}^{-1} \begin{bmatrix} -\frac{R_{sh\_ch}\times I_O}{R_{sh\_cap}+R_{sh\_ch}} \\ I_O\left(1-\frac{R_{sh\_ch}}{R_{sh\_cap}+R_{sh\_ch}}\right) \\ -I_O \\ 0 \end{bmatrix}$

Table I Six boundary conditions, the general solution for three current components ($I_{met}(x)$, $I_{cap}(x)$ and $I_{ch}(x)$), and their corresponding eigenvalues and eigenvectors.

Overall, R_S depends on the ohmic contact resistivity, the sheet resistances of the cap and QW channel layers, the barrier tunneling resistivity, and the lengths of the gate-to-source region and side-recessed regions.

EXPERIMENTAL RESULTS AND DISCUSSION

Two types of TLM structures were fabricated, as shown in **Fig. 3** such as the cap-only TLM structure (*cap-TLM*, (**a**)) to evaluate the contact characteristics of the non-alloyed ohmic metal stack, and the recessed TLM structure (*r-TLM*, (**b**)) which is identical to the real device without a Schottky gate electrode. Details on the epitaxial layer design and device processing were reported in our previous paper [4]. All the device processing was conducted on a full 3-inch wafer with an i-line stepper to ensure fine alignment accuracy within 0.05 µm. In the *r-TLM*, we varied L_g from 40 µm to 0.5 µm and L_{gs} from 10 µm to 0.2 µm. In this way, the split of L_g yielded the sheet resistance of the QW channel (R_{sh_ch}) from the linear dependence, and the source resistance (R_S) from the *y*-intercept at a given L_{gs}. Lastly, we investigated the dependence of R_S on L_{gs} in detail.

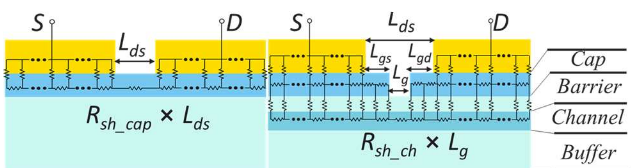

(a) (b)

Figure 3 Cross-sectional schematic of *cap-TLM* **(a)** and *r-TLM* **(b)** test structures.

Figure 4 (a) plots the measured total resistance (R_T) against L_{ds}, which corresponds to the length between the edge of source and the edge of drain, for the fabricated *cap-TLM* structures. This yielded values of R_{sh_cap} = 131 Ω/□, R_C = 32 Ω·µm, L_{T_cap} = 0.34 µm and ρ_c = 15 Ω·µm^2, with an excellent correlation coefficient of 0.99999. **Figure 4 (b)** plots the measured R_T against L_g for the *r-TLM* structures with various dimensions of L_{gs} from 10 µm to 0.2 µm. When L_g was long enough, each *r-TLM* device yielded approximately the same slope for all L_{gs} with excellent correlation coefficient. Since we designed the symmetrical L_{gs} and L_{gd}, half of the *y*-intercept from **Fig. 5 (a)** corresponded exactly to R_S. In analyzing *r-TLM* structures with various L_{gs}, values of the

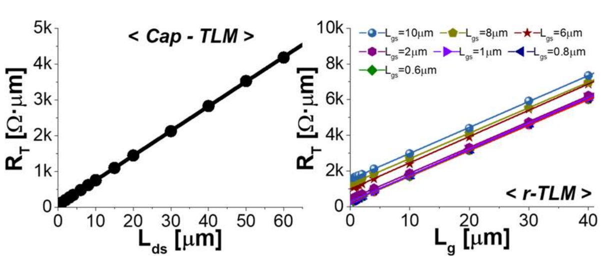

(a) (b)

Figure 4 (a) Measured R_T against L_{ds} for cap-TLM and **(b)** against L_g for *r-TLM*.

correlation coefficient were also greater than 0.999, increasing the credibility of the overall TLM analysis.

Figure 5 (b) plots the measured R_S (filled symbols) from the *r-TLM* analysis against L_{gs}, as well as the projected R_S (line) from Equation (5) with the model parameters of $\rho_{barrier}$ = 91 Ω·µm^2 and the others directly from the *cap-TLM* and *r-TLM* test structures. Additionally, the open symbols in **Figure 6** came from the R_S extracted directly from the reported HEMTs [4] using the gate-current injection technique [21]. There are two points to identify in **Fig. 6**. First, all the measured R_S characteristics were explained by the modeled R_S. Second, R_S was linearly proportional to L_{gs} for L_{gs} > 1 µm, where its slope was 69 Ω/. Interestingly, this was close to the parallel connection of R_{sh_cap} and R_{sh_ch}. However, this linear dependence of R_S on L_{gs} was no longer valid for L_{gs} < 1 µm and, most importantly, the measured R_S eventually saturated to approximately 123 Ω·µm even with L_{gs} approaching 0. Our model clearly indicated that this was because of the barrier tunneling resistivity. The saturation of R_S in L_{gs} = 0 was because the necessary lateral length for the cap-to-channel tunneling was supplied by its equivalent transfer length from

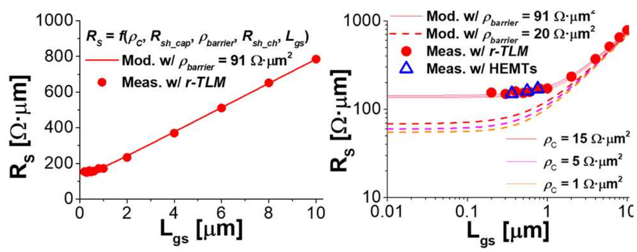

(a) (b)

Figure 5 Comparison of the modeled and measured R_s against L_{gs}; **(a)** in the *linear-linear* scale and **(b)** in the *log-log* scale.

the leading edge of the source metal contact ($-L_{T\_barrier} < x <$ 0) in Region-I.

Finally, let us discuss how to further reduce R_S with the R_S model proposed in this work. The three solid lines in **Fig. 6** are the model projections of R_S with the ohmic contact resistivity improve from 15 Ω·µm^2 (present) to 1 Ω·µm^2. Surprisingly, R_S would not be minimized that much even with a significant reduction in ρ_c and L_{gs} because of the $\rho_{barrier}$. Alternatively, the three dashed lines in Fig.5 are from the same model projection, but with $\rho_{barrier}$ = 20 Ω·µm^2. Note that a reduction in the $\rho_{barrier}$ is critical; in consequence, the projected R_S would be significantly scaled down to 70 Ω·µm and below. Under this circumstance, R_S could then be further reduced by the improved ohmic contact characteristics and the reduction of L_{gs}.

CONCLUSIONS

A fully analytical and physical investigation on R_S in advanced $In_xGa_{1-x}As$ QW HEMTs was carried out with a three-layer TLM system. Analytical solutions to the three current components (source metal, cap, and channel) along the selected coordinate system with appropriate boundary conditions were derived. The proposed R_S model in this work required only six physical and geometrical parameters (ρ_c, $\rho_{barrier}$, R_{sh_cap}, R_{sh_ch}, L_{side} and L_{gs}), yielding excellent agreement with the R_S values measured from the two TLM devices and previously reported $In_xGa_{1-x}As$ QW HEMTs. The developed model in this work could explain the saturation behavior of R_S for L_{gs} < 1 μm, which was due to the $\rho_{barrier}$. Therefore, one must pay a more careful attention to cut down the $\rho_{barrier}$ to further minimize R_S in future HEMTs.

ACKNOWLEDGEMENTS

This work was supported under the framework of international cooperation program managed by National Research Foundation of Korea (2022M3I8A1078437).

REFERENCES

[1] S. Amakawa *et al.*, “White Paper on RF enabling 6G–opportunities and challenges from technology to spectrum,” no. 13. University of Oulu, 2021.

[2] M. Ikram2022, "A Road towards 6G Communication—A Review of 5G Antennas, Arrays, and Wearable Devices" *Electronics* 11, no. 1: 169. https://doi.org/10.3390/electronics11010169.

[3] S. Cherry, "Edholm's law of bandwidth," in *IEEE Spectrum*, vol. 41, no. 7, pp. 58-60, July 2004, doi: 10.1109/MSPEC.2004.1309810.

[4] H. -B. Jo *et al.*, "L_g = 19 nm $In_{0.8}Ga_{0.2}As$ composite-channel HEMTs with f_T = 738 GHz and f_{max} = 492 GHz," *2020 IEEE International Electron Devices Meeting (IEDM)*, 2020, pp. 8.4.1-8.4.4, doi: 10.1109/IEDM13553.2020.9372070.

[5] C. M. Cooke *et al.*, "A 670 GHz Integrated InP HEMT Direct-Detection Receiver for the Tropospheric Water and Cloud Ice Instrument," in *IEEE Transactions on Terahertz Science and Technology*, vol. 11, no. 5, pp. 566-576, Sept. 2021, doi: 10.1109/TTHZ.2021.3083939.

[6] A. Leuther *et al.*, "20 nm metamorphic HEMT with 660 GHz f_T," *IPRM 2011 - 23rd International Conference on Indium Phosphide and Related Materials*, 2011, pp. 1-4.

[7] S.-W. Yun *et al.*, "$In_xGa_{1-x}As$ quantum-well high-electron-mobility transistors with a record combination of f_T and f_{max}: From the mobility relevant to ballistic transport regimes," *2021 IEEE International Electron Devices Meeting (IEDM)*, 2021, pp. 11.3.1-11.3.4, doi: 10.1109/IEDM19574.2021.9720667.

[8] T. Takahashi *et al.*, "Enhancement of f_{max} to 910 GHz by Adopting Asymmetric Gate Recess and Double-Side-Doped Structure in 75-nm-Gate InAlAs/InGaAs HEMTs," in *IEEE Transactions on Electron Devices*, vol. 64, no. 1, pp. 89-95, Jan. 2017, doi: 10.1109/TED.2016.2624899.

[9] P. J. Tasker and B. Hughes, "Importance of source and drain resistance to the maximum f_T of millimeter-wave MODFETs," in *IEEE Electron Device Letters*, vol. 10, no. 7, pp. 291-293, July 1989, doi: 10.1109/55.29656.

[10] K. Shinohara *et al.*, "547-GHz f_T $In_{0.7}Ga_{0.3}As$-$In_{0.52}Al_{0.48}As$ HEMTs with reduced source and drain resistance," in *IEEE Electron Device Letters*, vol. 25, no. 5, pp. 241-243, May 2004, doi: 10.1109/LED.2004.826543.

[11] E.-Y. Chang *et al.*, "InAs thin-channel high-electron-mobility transistors with very high current-gain cutoff frequency for emerging submillimeter-wave applications." *Applied Physics Express* 6.3 (2013): 034001.

[12] H.-B. Jo *et al.*, "Sub-30-nm $In_{0.8}Ga_{0.2}As$ Composite-Channel High-Electron-Mobility Transistors With Record High-Frequency Characteristics," in *IEEE Transactions on Electron Devices*, vol. 68, no. 4, pp. 2010-2016, April 2021, doi: 10.1109/TED.2020.3045958.

[13] X. Mei *et al.*, "First Demonstration of Amplification at 1 THz Using 25-nm InP High Electron Mobility Transistor Process," in *IEEE Electron Device Letters*, vol. 36, no. 4, pp. 327-329, April 2015, doi: 10.1109/LED.2015.2407193.

[14] D.-Y. Yun *et al.*, "Impact of the Source-to-Drain Spacing on the DC and RF Characteristics of InGaAs/InAlAs High-Electron Mobility Transistors," in *IEEE Electron Device Letters*, vol. 39, no. 12, pp. 1844-1847, Dec. 2018, doi: 10.1109/LED.2018.2876709.

[15] Crook, Adam M *et al.*, "Low resistance, nonalloyed Ohmic contacts to InGaAs." *Applied Physics Letters* 91.19 (2007): 192114.

[16] N. Waldron, D.-H. Kim and J. A. del Alamo, "A Self-Aligned InGaAs HEMT Architecture for Logic Applications," in *IEEE Transactions on Electron Devices*, vol. 57, no. 1, pp. 297-304, Jan. 2010, doi: 10.1109/TED.2009.2035031.

[17] D. A. J. Moran, H. McLelland, K. Elgaid, G. Whyte, C. R. Stanley and I. Thayne, "50-nm Self-Aligned and “Standard” T-gate InP pHEMT Comparison: The Influence of Parasitics on Performance at the 50-nm Node," in *IEEE Transactions on Electron Devices*, vol. 53, no. 12, pp. 2920-2925, Dec. 2006, doi: 10.1109/TED.2006.885674.

[18] T. Takahashi, M. Sato, K. Makiyama, T. Hirose and N. Hara, "InAlAs/InGaAs HEMTs with Minimum Noise Figure of 1.0 dB at 94 GHz," *2007 IEEE 19th International Conference on Indium Phosphide & Related Materials*, 2007, pp. 55-58, doi: 10.1109/ICIPRM.2007.381121.

[19] J. Jeong *et al.*, "3D stackable cryogenic InGaAs HEMTs for heterogeneous and monolithic 3D integrated highly scalable quantum computing systems," *2022 IEEE Symposium on VLSI Technology and Circuits (VLSI Technology and Circuits)*, 2022, pp. 328-329,doi: 10.1109/VLSITechnologyandCir46769.2022.9830449.

[20] Feuer, M.D. Two-layer model for source resistance in selectively doped heterojunction transistors. *IEEE Trans. Electron. Devices* **1985**, *32*, 7–11.

[21] Azzam, W.J.; Del Alamo, J.A. An all-electrical floating-gate transmission line model technique for measuring source resistance in heterostructure field-effect transistors. *IEEE Trans. Electron. Devices* 1990, *37*, 2105–2107.

ACRONYMS

QW: Quantum-Well
HEMT: High-electron-mobility transistor
TLM: Transmission-line model